



Measurement of three-photon excitation cross-sections of fluorescein from 1154 nm to 1500 nm

AARON K. LAVIOLETTE,* DIMITRE G. OUZOUNOV, AND CHRIS XU 

School of Applied and Engineering Physics, Cornell University, Ithaca, NY 14853, USA

*akl76@cornell.edu

Abstract: Measurements of three-photon action cross-sections for fluorescein (dissolved in water, pH ~11.5) are presented in the excitation wavelength range from 1154 to 1500 nm in ~50 nm steps. The excitation source is a femtosecond wavelength tunable non-collinear optical parametric amplifier, which has been spectrally filtered with 50 nm full width at half maximum band pass filters. Cube-law power dependance is confirmed at the measurement wavelengths. The three-photon excitation spectrum is found to differ from both the one- and two-photon excitation spectra. The three-photon action cross-section at 1154 nm is more than an order of magnitude larger than those at 1450 and 1500 nm (approximately three times the wavelength of the one-photon excitation peak), which possibly indicates the presence of resonance enhancement.

© 2023 Optica Publishing Group under the terms of the [Optica Open Access Publishing Agreement](#)

1. Introduction

Long wavelength three-photon fluorescence microscopy is advantageous for deep tissue imaging mainly because tissue scattering is typically reduced at long wavelengths. Three-photon excitation reduces out-of-focus background and the long wavelength windows are compatible with existing blue, green and red fluorophores. Since the first demonstration of deep tissue imaging in the early 2010's [1], long wavelength three-photon microscopy is increasingly being used for deep in vivo brain imaging, including in the mouse brain through cranial windows [2,3], through the intact and un-thinned mouse skull [4], and in freely moving mice [5,6] as well as rats [7]. Other organisms such as fish [8,9], and flies [10] have been examined, as well as other tissues such as the lymph nodes [11] and tumors [12]. Advanced techniques such as adaptive optics [13–16] and adaptive excitation [17] can also be combined with three-photon imaging, and several companies now offer commercial lasers and microscopes for three-photon imaging.

In the past decade much work has been done to characterize three-photon microscopy including measurement of tissue properties [1,18,19] and quantification of how to judge images (for example with the d' parameter [20] or the binary detection factor [21]). A critical parameter in three-photon microscopy is the absolute value of a fluorophore's three-photon cross-section. To guide and optimize quantitative deep tissue imaging, measurements of absolute three-photon cross-sections across a large wavelength range (particularly in the long wavelength range of >1100 nm) are needed.

Unlike two-photon microscopy, reference standards for three-photon cross-sections have not been established in peer-reviewed literature (i.e., measurement of the absolute cross-section of a fluorophore over a large spectral range). While there are reports of three-photon cross-sections in peer-reviewed literature, previous measurements have either been made in the short wavelength range (<1050 nm) [22,23], were only made at one or a few select wavelengths [24–28], use non-standard reference molecules (uncommon, or fluorescent proteins) [29–33], and/or have only looked at red fluorophores in specific wavelength windows [29,31–33]. Thus, while there are several past attempts in measuring three-photon cross-sections, no reliable reference standard

for three-photon excitation has been established, particularly in the long wavelength excitation windows for deep tissue imaging.

Direct measurement of a three-photon cross-section is difficult because only a small fraction of the excitation photons are absorbed in the three-photon process. More relevant for three-photon fluorescence microscopy is the determination of the three-photon action cross-section (i.e., the product of the cross-section and the fluorescence quantum efficiency). Although the fluorescence method provides much better sensitivity, accurate measurement requires precise knowledge of the temporal and spatial profile of the excitation light. Furthermore, measurements above ~ 1100 nm, where solvent (e.g., water) absorption is no longer negligible, introduce additional complexities typically not considered below ~ 1100 nm.

In this paper, we measured the three-photon action cross-section of fluorescein in water (with a small amount of NaOH to make the pH ~ 11.5) in an epi-fluorescence microscope setup. We used a low repetition rate (~ 400 kHz) excitation source, which enabled us to achieve pure three-photon excitation at wavelengths as short as 1154 nm. Our data spans from 1154 to 1500 nm in ~ 50 nm steps, which is sufficient for imaging applications due to the large spectral width of the femtosecond excitation pulses. Unlike other fluorophores previously measured at short wavelengths and over a narrow range [22], we found that the shape of the three-photon excitation spectrum of fluorescein differs substantially from its one-photon excitation spectral shape. The three-photon action cross-section at 1154 nm is more than an order of magnitude larger than those at 1450 and 1500 nm (approximately three times the wavelength of the one-photon excitation peak), which possibly indicates the presence of resonance enhancement [29,34].

2. Analysis of the multiphoton excitation of fluorophores

Multiphoton excitation of fluorophores is a function of both space and time for which the theory has been worked out previously [35,36]. In the absence of saturation (i.e., ground state depletion), the time averaged fluorescence power collected from a sample, $\langle F(t) \rangle$ (i.e., photons/second) is given as

$$\langle F(t) \rangle = \frac{1}{n} g^{(n)} \phi C \eta \sigma_n \langle I_0(t) \rangle^n \int_V S^n(\mathbf{r}) d\mathbf{r} \quad (1)$$

where n is the order of excitation, $g^{(n)}$ is the n^{th} order coherence at zero delay, ϕ is the system collection efficiency, η is the fluorophore's quantum efficiency, σ_n is the fluorophore's n^{th} order cross-section (i.e., $\eta \sigma_n$ is the action cross-section), C is the fluorophore concentration, $I_0(t)$ is the excitation intensity at the geometric focus, and $S(\mathbf{r})$ is the spatial distribution of the excitation light (defined such that $S(\mathbf{r} = \mathbf{0}) = 1$) [35,36].

In this study water will be used as a solvent. Water absorption at certain wavelengths (e.g., 1450 nm) is high and must be accounted for. Correcting for the power loss between the sample surface and the focus is done with the Beer-Lambert law. That is, if $P(t)$ is the power at the sample focus then $P(t) = P_s(t) \exp(-\alpha \Delta z)$, where $P_s(t)$ is the power at the surface, α is the absorption coefficient, and Δz is the distance between the surface and focus. Δz can be measured by moving a translation stage and taking the focal elongation into account, i.e.,

$$\Delta z = \Delta z_s \frac{\tan(\sin^{-1}(\text{NA}))}{\tan(\sin^{-1}(\text{NA}/n_0))} \approx \Delta z_s n_0 \quad (2)$$

where Δz_s is the distance the stage moved, NA is the numerical aperture of the focusing lens, and n_0 is refractive index of the sample (we have assumed that a dry focusing lens is used). Eq. (2) can be readily derived via ray optics, and the approximation is valid for low NA.

In addition to accounting for the loss between the sample surface and focus, $S(\mathbf{r})$ also needs to account for the loss due to the spatial distribution of light at the focus (which in this case is a

diffraction limited focus). For low NA lenses, we approximate the loss as only occurring along the optic axis and model the loss via the Beer-Lambert law. Thus,

$$S(\mathbf{r}) = h^2(u, v) \exp(-\alpha z) \quad (3)$$

where z is the direction along the optical axis, and $h^2(u, v)$ is the paraxial form of the normalized intensity point spread function (PSF) given by [35,36],

$$h^2(u, v) = \left| 2 \int_0^1 J_0(v\theta) \exp\left(-\frac{1}{2}iu\theta^2\right) \theta d\theta \right|^2 \quad (4)$$

where u and v are optical coordinates defined as

$$v = \frac{2\pi\text{NA}\rho}{\lambda} \quad (5)$$

and

$$u = \frac{2\pi\text{NA}^2 z}{n_0\lambda} \quad (6)$$

with ρ being the distance away from the optic axis and λ the (vacuum) excitation wavelength. We note that in Eq. (3), z is defined such that $z = 0$ corresponds to the geometric focus in the absence of loss, and increasing z points in the direction away from the surface.

For convenience we define the parameter $\beta \equiv \alpha n_0\lambda/(2\pi\text{NA}^2)$ so that

$$\int_V S^n(\mathbf{r}) d\mathbf{r} = b_n \left[\frac{n_0\lambda^3}{8\pi^3\text{NA}^4} \right] \quad (7)$$

with

$$b_n = \int_0^\infty 2\pi v dv \int_{-\infty}^\infty h^{2n} \exp(-\beta n u) du. \quad (8)$$

The integral is solved numerically using MATLAB as a function of β . When $\beta = 0$ we find that $b_3 = 28.07$ which is in agreement with the value of 28.1 as previously published [35]. For $\beta \neq 0$, $b_3 \geq 28.07$ as the loss effectively “enlarges” the PSF. However, for this study the largest value of b_3 is 28.29, which is <1% more than 28.1. This is expected since the propagation loss over a distance comparable to the axial resolution of a diffraction limited focus is small. Additionally, we note that this small change in b_3 is an advantage for measuring three-photon cross-sections in a microscopy setup, as compared to a non-focused system, because the loss in the latter case would significantly affect the region where fluorescence occurs (e.g., across the entire sample cuvette).

Noting that for a diffraction limited focus the intensity at the geometric focus can be written in terms of the power at the geometric focus (P) as

$$I_0(t) = \frac{\pi\text{NA}^2}{\lambda^2} P(t), \quad (9)$$

and that $g^{(n)}$ can be written as

$$g^{(n)} = g_p^{(n)} / (f\tau)^{(n-1)} \quad (10)$$

where f is the laser repetition-rate, τ is the pulse full width at half maximum (FWHM), and $g_p^{(n)}$ is a dimensionless quantity depending on the shape of the temporal intensity profile, Eq. (1) can

then be re-written for three-photon fluorescence as

$$\langle F(t) \rangle = \frac{1}{3} \frac{g_p^{(3)}}{(f\tau)^2} \phi C \eta \sigma_3 n_0 \frac{b_3 \text{NA}^2 \langle P(t) \rangle^3}{8\lambda^3}. \quad (11)$$

Likewise for two-photon fluorescence,

$$\langle F(t) \rangle = \frac{1}{2} \frac{g_p^{(2)}}{f\tau} \phi C \eta \sigma_2 n_0 \frac{b_2 \langle P(t) \rangle^2}{8\pi\lambda}. \quad (12)$$

For two-photon fluorescence we took b_2 as 64 (the same value without considering propagation loss in the solvent).

3. Experimental methods

3.1. Experimental setup

The experimental setup is shown in Fig. 1. Briefly, the excitation source, a noncollinear optical parametric amplifier (NOPA, Spectra Physics; repetition rate 402.3 ± 0.3 kHz; used for three-photon measurements) pumped by an amplifier (Spirt, Spectra Physics) or a Titanium:Sapphire (Ti:S) oscillator (Spectra Physics Tsunami; repetition rate of 81.97 ± 0.01 MHz; used for two-photon measurements) pumped by a diode-pumped solid-state laser (SproutG, Lighthouse Photonics), is passed through two reflective continuously variable neutral density (ND) filter wheels (NDC-50C-4 M, ThorLabs), which serve as power control. The maximum pulse energy from the NOPA (before attenuation by the ND filters) is $\sim 1 \mu\text{J}$. For the cross-section measurements, the two flipper mirrors (abbreviated FM) are in the “up” position to direct the laser through a long pass (LP) filter or band pass filter (BPF). The LP filter is a 715 LP (FF01-715/LP-25, Semrock) when the Ti:S oscillator is used. For the NOPA, a set of 50 nm FWHM BPFs (centered at 50 nm increments from 1150 to 1500 nm) were used (#85-895, #85-896, #85-897, #85-898, #85-899, #85-900, #85-901, #85-902, Edmund Optics). The BPFs were used because the NOPA had a very large spectral bandwidth (~ 100 nm FWHM for certain wavelengths), and since spectroscopy measurements are being done, we decided to narrow the bandwidth with the BPFs to have a more precise handle on the excitation wavelength.

The LP or BPFs are placed on the outside of a light tight enclosure and help to keep out any stray visible light (including any third harmonic generation (THG) propagating along with the beam). From here the laser is directed through -15 mm (LD2060, Thorlabs) and 150 mm (LA1417, Thorlabs) focal length lenses (which are uncoated). These two lenses serve as a 10x beam expander, which expands the beam to a $1/e^2$ diameter of approximately >18 mm for the Ti:S oscillator and approximately >30 mm for the NOPA. The expanded beam is passed through a 757 LP dichroic mirror (FF757-Di01, Semrock) and overfills an objective lens (UPlanFLN 10x/0.3, Olympus), which creates a diffraction limited focus in the sample (which is a fluorescein solution in a deep well side sealed with a piece of cover glass). Despite the fact that the lens has a nominal NA of 0.3, it has been previously measured to be 0.26 for infrared wavelengths [28]. The emitted light is then collected by the objective, redirected by the 757 LP dichroic mirror through a series of short pass (SP) filters (900 SP, FESH0900, Thorlabs, 800 SP, FESH0800, and 700 SP, FESH0700, Thorlabs) and a BPF (531/46, Brightline 531/46, Semrock) to an ultra-bialkali photomultiplier tube (PMT; R7600U-200, Hamamatsu). The PMT signal is then amplified by a 10 MHz trans-impedance amplifier (TIA: C9999, Hamamatsu) and recorded with a photon counter (SR400, Stanford Research Systems).

For determination of the power in the sample, the sample is placed on a stage that allows it to be moved out of the way, so the light that reaches the focus can be collected by an uncoated 11.25 mm focal length lens (KPA13, Newport), and directed to a power meter (S132C, Thorlabs).

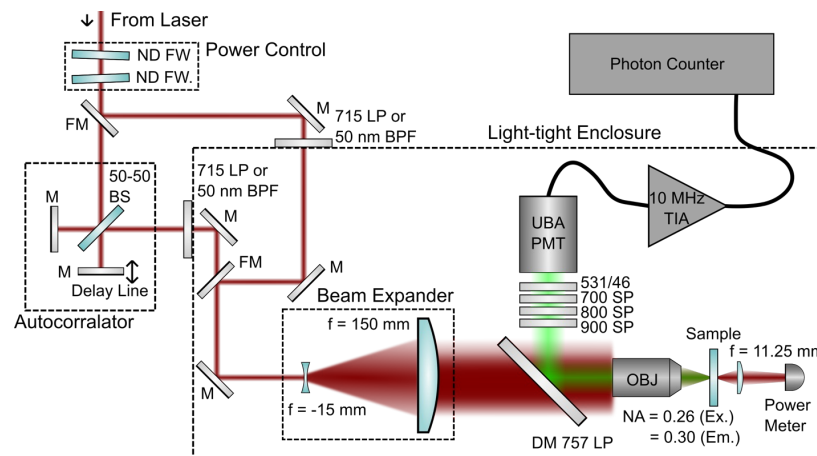


Fig. 1. Layout of the experimental setup. For the cross-section measurements the two flipper mirrors (FM) are placed in the “up” position so that the light bypasses the autocorrelator before entering the light tight enclosure (for pulse width measurements these are in the “down” position so the autocorrelator is used). The beam enters the light tight enclosure via a long pass LP filter (715 for the Ti:S) or BPF (for the NOPA). For the cross-section measurements the sample is placed on a movable stage, so the power after the objective can be determined by moving the sample out of the way and directing the beam into a power meter. Abbreviations: ND FW, neutral density filter wheel; FM, flipper mirror; M: mirror; BS, beam splitter; LP: long pass; SP: short pass; BPF: band pass filter; UBA PMT: ultra-bialkali photomultiplier tube; OBJ: objective lens; NA, numerical aperture; Ex., excitation; Em., emission; TIA; trans-impedance amplifier.

Knowing the transmission through the 11.25 mm lens, cover glass, and the loss due to solvent absorption between the surface and the focus, the power at the geometric focus can be calculated.

For measurement of the pulse width, the flipper mirrors are in the “down” position to direct the light through an interferometric autocorrelator, which uses a 50/50 beam splitter (BSW23R, Thorlabs) and a motorized stage (Z825B, Thorlabs). Although not shown, we also placed two pieces of cover glass in the horizontal arm, as we found that was necessary to make the power in each arm even. The sample is then replaced by either a GaAsP (G1116, Hamamatsu) or Si (S1223-01, Hamamatsu) photodiode, depending on the wavelength (using the GaAsP photodiode at wavelengths < 1275 nm). The two-photon generated photocurrent is amplified by a low noise amplifier (SR570, Stanford Research Systems). The control of the stage and recording of the data with a data acquisition card (NI9215, National Instruments) is done by a custom MATLAB program. The same LP or BPF was placed in the autocorrelator path when autocorrelation was being done.

The NOPA spectrum was measured by placing a single mode fiber (SM980-5.8-125, Thorlabs) with a cutoff wavelength of 980 nm at the focus of the objective and measuring the spectrum with a fiber input spectrometer (HP70951B, Hewlett-Packard). Again, the BPFs were used, and the power was varied to ensure no non-linear effects in the fiber. For the Ti:S oscillator, an Ocean Optics spectrometer (HR + D0678) was used, which was placed near the output of the Ti:S oscillator.

Not shown in Fig. 1 is that up-stream of the ND filters the NOPA passes through a 1064 LP filter (BLPOL-1064R-25, Semrock) and 1/2 wave plate (AHWP05M-1600, Thorlabs) which changes the polarization so it is horizontal to the table. Additionally, the Ti:S oscillator passes through a 1/2 wave plate (WPH05M-808, Thorlabs), an isolator (Model 714, ConOptics), and a second 1/2 wave plate (AHWP05M-980, Thorlabs). The first 1/2 wave plate rotates the polarization to

adjust the power which can pass through the isolator, and the second rotates the polarization after the isolator so it is horizontal to the table (just to be consistent with the beam from the NOPA).

3.2. Spectrum and pulse width measurement considerations

For determining the cross-sections, measurement of both the carrier wavelength and the pulse width are important considerations. For a NOPA with ultrashort pulses, generally the spectral bandwidth is quite large, and the spectrum typically has an irregular shape, even with filtering the spectrum as is done here (Fig. S1). We decided to use the “center of mass” definition of the carrier frequency [37]. That is, if $S(\nu)$ is the spectrum (not spectral density, i.e., units of W not W/Hz) as a function of frequency, ν , the carrier frequency, ν_0 , is defined as

$$\nu_0 = \frac{\int_{-\infty}^{\infty} \nu S(\nu) d\nu}{\int_{-\infty}^{\infty} S(\nu) d\nu} \quad (13)$$

and the carrier wavelength is simply $\lambda_0 = c/\nu_0$. We note the limits in Eq. (13) are approximated with appropriate finite limits.

The pulse width measurements then make use of this carrier wavelength as the time-delay axis was calibrated by considering the spacing between the peaks of the interferometric autocorrelation trace. The intensity autocorrelation was then recovered digitally via Fourier transforms [37], and the FWHM of the pulse was found from the FWHM of the intensity autocorrelation assuming a Gaussian pulse shape for the NOPA and a Sech² for the Ti:S oscillator. Additionally for the autocorrelation of the Ti:S oscillator, $g^{(2)}$ (and $g_p^{(2)}$) can be measured directly [35,38]. We found $g_p^{(2)} = 0.63$, which is close to the calculated value for a Sech² pulse shape of 0.59 (0.59 was used in subsequent calculations). For the Ti:S oscillator the FWHM of the pulse was ~219 fs and in the range of ~88 to ~131 fs for the NOPA (Fig. S2).

3.3. Collection efficiency considerations

A key component of measuring the cross-section is determining the collection efficiency, which is the ratio between the total amount of light emitted by the sample and the actual amount of light detected. In theory this can be determined by considering geometrical collection of the objective lens, the emission spectrum of fluorescein, transmission through all the optical elements and the quantum efficiency of the PMT, i.e.,

$$\phi = \Omega_f \frac{\int_0^{\infty} s(\lambda) q(\lambda) \prod_j T_j(\lambda) d\lambda}{\int_0^{\infty} s(\lambda) d\lambda} \quad (14)$$

where $s(\lambda)$ is the emission spectral density (i.e., W/nm) of fluorescein, $q(\lambda)$ is the PMT quantum efficiency, $T_j(\lambda)$ is the transmission of the j^{th} optical element between the fluorophore and PMT (including the cover glass/water interface, cover glass/air interface, objective lens, dichroic mirror, filters), and $\Omega_f = 0.5 \left(1 - \sqrt{1 - (\text{NA}/n_0)^2} \right)$ is the fractional solid angle as collected by the lens.

We calculated ϕ with Eq. (14) by using $s(\lambda)$ available from Semrock’s SearchLight tool [39], using $q(\lambda)$ provided by the PMT manufacture, measuring T_j for the filters and dichroic mirror (using a Cary 300 UV-Vis spectrometer), calculating T_j for the cover glass/air and cover glass/water interfaces based on the medium’s refractive indices and Fresnel’s equations at normal

incidence (the water index was taken from interpolating data reported by Segelstein [40], the cover glass index was found using the Sellmeier parameters of Schott NBK7 [41]), and assuming the fluorescence collection NA = 0.3. We found that $\phi = 0.1\%$.

As a check, we then measured the two-photon action cross-section (i.e., $\eta\sigma_2$) at 800 nm (using the Ti:S oscillator) and compared it to the literature value. We obtained a value of ~ 22 GM (1 GM = 10^{-50} cm⁴s). Previously Xu and Webb measured ~ 32 GM [36]. However, we note that they used a value of $g_p^{(2)} = 0.41$ (to make their measurements using continuous-wave and pulsed excitation match) [36], where we used $g_p^{(2)} = 0.59$. If Xu and Webb used 0.59 instead, they would have gotten ~ 22 GM. Song et al. measured ~ 49 GM [42], while Makarov et al. measured ~ 32 GM [43], and Reguardati et al. measured ~ 22 GM [44] (all assuming a quantum efficiency of 0.9 [36]), the last of which is closer to our number. However, given the potential discrepancies in the previous literature, we chose to use our calculated value for collection efficiency, but with a $\sim 50\%$ uncertainty, and so we quote the final number for the collection efficiency as $\phi = 0.1 \pm 0.05\%$.

3.4. Sample preparation

The fluorescein was purchased in powder form (Catalog No. 11924, Argos Organics) and a solution was prepared by dissolving the powder in water and a small amount of NaOH. Specifically, the solution was prepared by first making a ~ 500 mL solution of ~ 100 μ M fluorescein. The pH of the solution was brought to ~ 11.5 by adding in a small amount of a 1 M NaOH stock solution (which was made from NaOH pellets (No. 7708-06, Macron Fine Chemicals)). Then this solution was diluted to ~ 10 μ M, which would be used in this study.

The concentration of the solution was verified by using an absorption spectrometer (Cary 300 UV-Vis spectrometer). Specifically, a series of 10 dilutions were made to a portion of the ~ 10 μ M solution, and the absorbance was measured. The peak absorbance and relative concentration were fit to a linear regression model (without an intercept) and the slope, along with the known path length and molar extinction coefficient provided by the manufacture of the fluorescein, was used to back out the concentration. The final concentration of the solution was measured to be 10.49 ± 0.09 μ M. This number will be used for this study.

For cross-section measurements, the solution was placed into a deep well slide (MS15C1, ThorLabs), and sealed with a piece of #1.5 borosilicate cover glass (No. 3406, Thermo Scientific). The depth of the well is between 600 and 800 μ m.

3.5. Experimental procedure and data processing

Before taking data, we first positioned the sample, so the focus was a known distance from the cover glass/solvent interface. The location of this surface was found either from the presence of signal or looking for THG from the cover glass/solvent interface. The focus was positioned between 54 and 75 μ m (depending on the wavelength) behind the cover glass (by moving a translation stage). For all wavelengths a background beyond dark counts (when a sample with just solvent was placed in the setup) was not noticed at the powers used.

The photon counter was set to count for a period of 30 seconds. The large amount of time was chosen for an increased signal to noise ratio (SNR). For each excitation wavelength we began by counting the dark counts and recording the background (dark) power on the power meter, which would be used for background correction. Three trials of 30 seconds each were taken, and the data averaged. Then the laser was allowed to enter the box and data taken at seven different power levels. The power at the focus was determined by moving the sample out of the way, recording the power on the power meter, and then correcting for the transmission of the 11.25 mm lens, the cover glass/air and cover glass/water interfaces, and the loss in the sample.

We then processed the data in two steps. First, we plotted the recorded power on the power meter vs. the recorded counts on a log-log scale and fit the data to a linear model of the form $\log_{10}(F_M) = c_1 \log_{10}(\langle P_M \rangle) + c_2$ where F_M is the measured (background corrected) counts and

$\langle P_M \rangle$ is the measured average (background corrected) power on the power meter. The purpose of this was to check that the power dependence of the fluorescence (i.e., the slope c_1) is correct. Once this was confirmed we fit the three-photon data to an equation of the form $F_M = c_3 \langle P_M \rangle^3$ and the cross-section is backed out from c_3 , i.e.,

$$\eta\sigma_3 = \frac{24f^2\tau^2\lambda_0^3c_3}{b_3g_p^{(3)}\phi Cn_0NA^2T_{cnt}T_{cal}^3} \quad (15)$$

where T_{cnt} is the count time (in this case 30 seconds) and T_{cal} is the calibration factor that allows the power at the focus to be found from multiplying it with the measured power on the power meter. In particular $T_{cal} = T_{CG/air}T_{CG/water}T_{loss}/T_{KPA13}$, where $T_{CG/air}$ and $T_{CG/water}$ are the transmission through the cover glass/air and cover glass/water interfaces, T_{KPA13} is the transmission through the 11.25 mm lens, and T_{loss} represents the loss incurred by traveling through the water and is calculated from the Beer-Lambert law at the carrier wavelength and with data for the complex index of refraction of water interpolated from data reported by Segelstein [40]. Similarly this data is used along with the Sellmeier parameters for Schott NBK7 [41] and Fresnel equations at normal incidence to find $T_{CG/water}$ and $T_{CG/air}$. T_{KPA13} is found in a similar way except we used Sellmeier parameters for Ohara L-BAL35 [45], since the 11.25 mm lens is made from this glass.

For the two-photon data a similar procedure is followed except the fitting equation is now $F_M = c_3 \langle P_M \rangle^2$ and

$$\eta\sigma_2 = \frac{16f^2\tau\lambda_0c_3}{b_2g_p^{(2)}\phi Cn_0T_{cnt}T_{cal}^2}. \quad (16)$$

4. Results

4.1. Power cubed (and squared) dependence

As discussed in the methods section, we first validated that the data followed a cube-law dependence with the power (or a square-law dependence in the case of the two-photon data). There are two main reasons for doing this. First it serves as a check that we are measuring a signal of the appropriate nonlinear order. Second, as previously shown, it is possible to measure a mixed two- and three-photon signal at certain wavelengths and we wanted to make sure that this was not the case [22,29]. This was confirmed by plotting F_M against $\langle P_M \rangle$ on a log-log scale and finding the “slope” as is shown in Fig. 2 for the power levels used in our measurements.

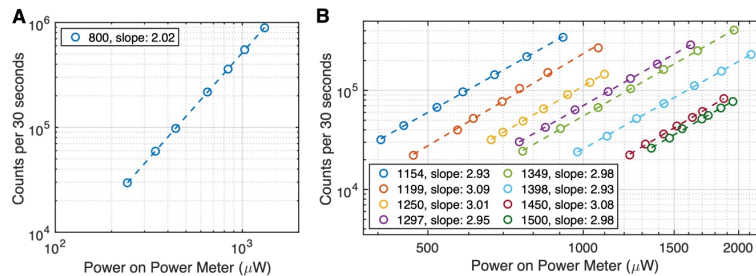


Fig. 2. Power dependence curves. The power dependence for two-photon (A) and three-photon (B) excitation wavelengths. The circles are the data points, and the dashed line is a least-squares fit. The wavelengths and fitted slopes are indicated in the legend. The standard errors of the slopes shown are less than $\pm 3\%$. All count and power data shown here has been background corrected.

As can be seen from Fig. 2(A), the two-photon data follows a nearly perfect square-law dependance only differing from the ideal square-law by $\sim 1\%$. Likewise, the three-photon data (Fig. 2(B)) follows a nearly perfect cube-law dependence. The largest deviation across all the data is $\sim 3\%$, confirming that we were measuring a nonlinear signal of the correct order and that all three-photon data presented is dominated by a three-photon signal (i.e., the measured signal is for all practical purposes strictly from three-photon excitation).

4.2. Three-photon action cross-sections

The measured three-photon action cross-sections are presented in Table 1. Additionally, we plot the action cross-sections on both a liner (Fig. 3(A)) and semi-log (Fig. 3(B)) scale, along with the one- and two-photon cross-sections as a function of wavelength. The one-photon data is from an absorption spectrometer (Cary 300 UV-Vis) and scaled so the peak matches the peak data point quoted by the manufacture. The two-photon data is digitized from Xu and Webb [35].

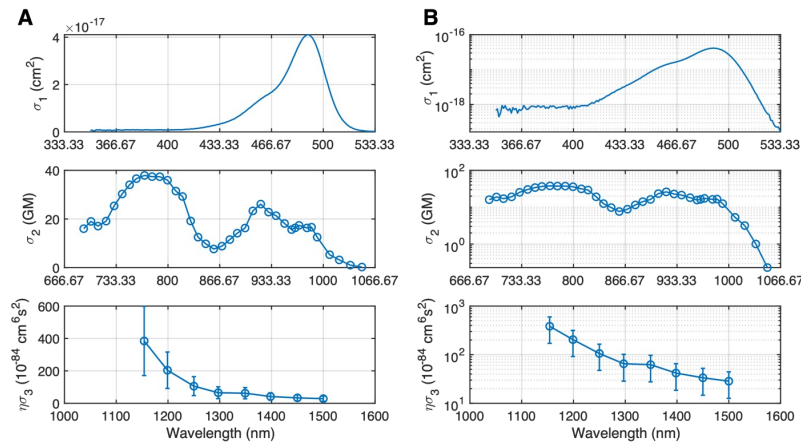


Fig. 3. One-, two-, and three-photon cross-sections compared. The one-, two-, and three-photon cross-sections are shown on both a liner (A) and semi-log (B) scale. The one-photon data is measured using an absorption spectrometer and scaled so the peak matches the manufacturer's quoted peak. The two-photon data is from Xu and Webb [35].

Table 1. Three-photon action cross-sections

Wavelength (nm)	Action Cross-Section ($10^{-84} \text{ cm}^6 \text{ s}^2$)
1154	385 ± 214
1199	204 ± 112
1250	106 ± 58
1297	65 ± 37
1349	62 ± 35
1398	42 ± 23
1450	34 ± 19
1500	29 ± 16

As can be seen in Fig. 3, the three-photon cross-sections are larger for shorter wavelengths, likely due to resonance enhancement (i.e., when the combined energy of two of the three excitation photons is close to the energy gap between the ground and first excited state, the three-photon

cross-section is possibly enhanced [29,34]). We were still able to obtain a cube-law dependence at 1154 nm. Although we were unable to reach ~1100 nm or shorter with our NOPA, it would be interesting to measure the cross-section at and below ~1100 nm in the future.

In comparison to one- and two-photon cross-sections, we see that the shape of the spectrum is much different than simply tripling the one-photon wavelength and different than multiplying the two-photon wavelength by 3/2 (although less so than the one-photon case). Therefore, the idea that one-photon and three-photon excitation might have the same spectral shape does not hold for fluorescein. Interestingly we do not see evidence of a three-photon cross-section peak around 1470 nm ($=490 \times 3$), even though a local maximum is observed in the two-photon data around 980 nm ($=490 \times 2$). It is possible this is because we didn't measure this point and the peak is subtle.

Despite the differences in the one-, two-, and three-photon spectral shapes, the three-photon action cross-sections presented here establish a reference that can be used for other fluorophores. We note that the simplicity of preparation (i.e., fluorescein can be bought as a powder and is water soluble), availability, and cost makes fluorescein an ideal candidate for this. We also caution that for three-photon microscopy, where generally pulses with a larger spectral bandwidth are used, the apparent three-photon cross-sections may be slightly different. Based on preliminary data without using the BPFs, we estimate this could be different by a factor of ~2.

4.3. Comparison with other data

Quantum perturbation theory suggests that the three-photon cross-section should be on the order of $\sim 10^{-82} \text{ cm}^6 \text{ s}^2$ [35], which our data agrees with. Unfortunately, there are only a few papers in literature for which to compare exact values with. Cheng et al. [28] measured the three-photon action cross-section of fluorescein at 1300 nm to be $\sim 16 \pm 5 \times 10^{-84} \text{ cm}^6 \text{ s}^2$ in an epi-based microscope setup, which is within the same order of magnitude reported in this study.

Rebane and Mikhaylov [46] have measured fluorescein (as well as other fluorophores) and presented their results in a conference proceeding manuscript. Their method used an unfocused beam passing through a cuvette, collected fluorescence at 90-degrees with a spectrometer, and determined the absolute three-photon cross-section by calibration against the known one- and two-photon cross-sections. However, for fluorescein the calibration against the one- and two-photon cross-sections results in an order of magnitude disagreement in their data for the three-photon cross-section. In addition, their data has a large peak at ~1450 nm which coincides with the water absorption peak [40,46]. We believe this peak is likely an artifact and a result of an overestimate of the correction for water absorption, which they did by dividing by the transmittance through the entire cuvette sample [46].

Despite this, Rebane and Mikhaylov [46] list in the text that they estimate the absolute three-photon cross-section of fluorescein at 1300 nm to be $\sim 30 \pm 15 \times 10^{-84} \text{ cm}^6 \text{ s}^2$ (corresponding to an action cross-section of $\sim 27 \pm 14 \times 10^{-84} \text{ cm}^6 \text{ s}^2$ assuming a quantum efficacy of 0.9 [36]), which when considering the uncertainty, is close to our number.

4.4. Other considerations

The presence of third harmonic generation (THG), from the optics or solvent, can be a concern when measuring three-photon cross-sections [46]. Because of the bandpass filter in front of the PMT, direct detection of THG is not a concern in our experiment. On the other hand, THG could excite fluorescein through the one-photon absorption process. To quantify this, we replaced the filters in front of the PMT with an infrared (IR) blocking filter (TF1, Thorlabs, passes 375-650 nm), and we detected a signal at all three-photon excitation wavelengths when a sample of just solvent (i.e., a blank) was placed in the setup, which follows a cube-law power dependence ($\sim 3^{\text{rd}}$ order). We estimated the wavelength of the signal by using bandpass filters. By placing a 435/40 BPF (FF02-435/40-25 Semrock) in addition to the IR blocking filter a signal

was present when the NOPA was tuned to 1297 nm, but only a very weak signal when tuned to 1398 nm. In addition, no signal beyond dark counts was detected when the same filters used in the experiment (including the 531/46 BPF) were in front of the PMT for all the wavelengths used in our experiments. These results indicate that this signal is likely to be THG.

We now estimate the upper bound contribution due to one-photon fluorescence excited by this THG signal using the same detection efficiency of 0.1% for the THG, a peak molar extinction coefficient value of $80,000 \text{ M}^{-1}\text{cm}^{-1}$, a path length of $800 \mu\text{m}$ (maximum depth of the well), a quantum efficiency of 0.9, and the same collection efficiency for one- and three-photon excited fluorescence. This results in an $\sim 13\%$ overestimate at 1500 nm, $\sim 20\%$ at 1450 nm, $\sim 7\%$ at 1398 nm, $\sim 4\%$ at 1349 nm, and $< 2.2\%$ for all other three-photon excitation wavelengths. The uncertainties caused by one-photon fluorescence excited by the THG signal are small when compared to the uncertainties of the three-photon excitation cross-section measurements, particularly for wavelengths shorter than 1400 nm.

In addition to the THG, the large water absorption present at 1450 ($\alpha = 0.00315 \mu\text{m}^{-1}$) means a significant amount of the energy put into the sample by the excitation beam ($\sim 90\%$ for an $800 \mu\text{m}$ path length) is absorbed in the sample and dissipated as heat which could in turn raise the sample temperature. According to Schönle and Hell's model [47] (the axially invariant Gaussian approximation, assuming a thermal conductivity of 0.6 W/mK and volumetric heat capacity of $4.2 \text{ MJ/m}^3\text{K}$), after 30 seconds the temperature at the geometric focus will rise by $\sim 10 \text{ K}$ for the maximum power used here ($\sim 1.6 \text{ mW}$, at the geometric focus). This is a clear overestimate as it assumes infinite boundaries, an axially invariant Gaussian beam, and only radial conduction. On the other hand, a lumped parameter approach (ignoring the difference in thermal conductivity between the glass and the water, assuming a 1.57 mm slab with 9 mm radius faces, and a $10 \text{ W/m}^2\text{K}$ heat transfer coefficient [48] on both faces) yields a negligible temperature increase, which is a clear underestimate.

We note for these models, the temperature rises linearly with the incident power. On the other hand, all the data points at 1450 nm follow the cube-law dependence when varying the power at the geometric focus from $\sim 1.1 \text{ mW}$ to $\sim 1.6 \text{ mW}$ (see Fig. 2). This suggests that even if there was heating it is not affecting the results.

4.5. Blue-shifted three-photon cross-sections

In this work we were able to measure large three-photon cross-sections at wavelengths as low as 1154 nm. These large cross-sections on the blue side of 1470 nm (3 times the one-photon spectral peak) suggest that resonant enhancements may be occurring, and an inherent similarity between one- and three-photon absorption spectrum is not present in all fluorophores. Indeed, other works have also seen differences in the one- and three-photon spectral shapes for certain fluorophores [29,31,33,46], while others have not [30,36]. Therefore, it is difficult to predict three-photon cross-sections from their one-photon cross-sections, which was also frequently observed for two-photon cross-sections.

The ability to measure pure three-photon cross-sections as low as 1154 nm (as evidenced by the 3rd order power dependence) may also come as a surprise given that $\sim 100 \text{ nm}$ bluer two-photon cross-sections can be measured [36]. This however may be understood because we employed a low repetition rate ($\sim 400 \text{ kHz}$) excitation source. Assuming a diffraction limited focus, no loss, and the same average power, then the ratio of two-to-three-photon fluorescence scales as $f\tau\sigma_2/(\sigma_3\text{NA}^2)$. This means that if we were to use a high repetition rate source (e.g., $\sim 80 \text{ MHz}$ from a mode-locked laser), the ratio would be about 200 times larger than it was in this study, and likely very difficult to measure pure three-photon fluorescence here.

This ratio also implies that the repetition rate, pulse width and spatial confinement (i.e., the NA) can be changed to vary the ratio between two- and three-photon fluorescence as has been previously pointed out [22,29]. Additionally, the large blue-shifted three photon cross-sections

of fluorescein may make multicolor imaging with green and blue fluorophores possible as has already been demonstrated with green and red fluorophores [29]. However, the large cross-section and multicolor advantage may come at the expense of penetration depth into a mouse brain, as the effective attenuation for the excitation light is higher at shorter wavelengths [1,49].

5. Conclusion

The measurement of three-photon action cross-sections, from 1154 to 1500 nm in ~50 nm steps, for fluorescein (dissolved in water, pH ~11.5) was presented. For all wavelengths considered here we were able to confirm cube-law power dependence even in the bluer wavelengths, likely due to the use of a low repetition rate system. The three-photon excitation spectrum is found to differ from both the one- and two-photon excitation spectra, with the three-photon spectrum showing very large cross-sections at short wavelengths and the lack of a peak around ~1470 nm (3x the one-photon peak). The results presented here can be used as a reference for measuring the absolute three-photon cross-sections of other fluorophores within the same wavelength range.

Funding. National Science Foundation (DBI-1707312); National Institutes of Health/National Institute of Biomedical Imaging and Bioengineering (R01EB033179).

Acknowledgments. We thank Warren R. Zipfel for the use of his absorption spectrometer and the fruitful conversations.

Disclosures. The authors declare no conflicts of interest.

Data availability. Data underlying the results presented in this paper are not publicly available at this time but may be obtained from the authors upon reasonable request.

Supplemental document. See [Supplement 1](#) for supporting content.

References

1. N. G. Horton, K. Wang, D. Kobat, C. G. Clark, F. W. Wise, C. B. Schaffer, and C. Xu, "In vivo three-photon microscopy of subcortical structures within an intact mouse brain," *Nat. Photonics* **7**(3), 205–209 (2013).
2. D. G. Ouzounov, T. Wang, M. Wang, D. D. Feng, N. G. Horton, J. C. Cruz-Hernandez, Y.-T. Cheng, J. Reimer, A. S. Tolias, N. Nishimura, and C. Xu, "In vivo three-photon imaging of activity of GCaMP6-labeled neurons deep in intact mouse brain," *Nat. Methods* **14**(4), 388–390 (2017).
3. M. Yildirim, H. Sugihara, P. T. C. So, and M. Sur, "Functional imaging of visual cortical layers and subplate in awake mice with optimized three-photon microscopy," *Nat. Commun.* **10**(1), 1–12 (2019).
4. T. Wang, D. G. Ouzounov, C. Wu, N. G. Horton, B. Zhang, C.-H. Wu, Y. Zhang, M. J. Schnitzer, and C. Xu, "Three-photon imaging of mouse brain structure and function through the intact skull," *Nat. Methods* **15**(10), 789–792 (2018).
5. A. Klioutchnikov, D. J. Wallace, J. Sawinski, K. M. Voit, Y. Groemping, and J. N. D. Kerr, "A three-photon head-mounted microscope for imaging all layers of visual cortex in freely moving mice," *Nat. Methods* **20**(4), 610–616 (2023).
6. C. Zhao, S. Chen, L. Zhang, D. Zhang, R. Wu, Y. Hu, F. Zeng, Y. Li, D. Wu, F. Yu, Y. Zhang, J. Zhang, L. Chen, A. Wang, and H. Cheng, "Miniature three-photon microscopy maximized for scattered fluorescence collection," *Nat. Methods* **20**(4), 617–622 (2023).
7. A. Klioutchnikov, D. J. Wallace, M. H. Frosz, R. Zeltner, J. Sawinski, V. Pawlak, K. M. Voit, P. S. J. Russell, and J. N. D. Kerr, "Three-photon head-mounted microscope for imaging deep cortical layers in freely moving rats," *Nat. Methods* **17**(5), 509–513 (2020).
8. N. Akbari, R. L. Tatarsky, K. E. Kolkman, J. R. Fetcho, A. H. Bass, and C. Xu, "Whole-brain optical access in a small adult vertebrate with two- and three-photon microscopy," *iScience* **25**(10), 1–13 (2022).
9. D. M. Chow, D. Sinefeld, K. E. Kolkman, D. G. Ouzounov, N. Akbari, R. Tatarsky, A. Bass, C. Xu, and J. R. Fetcho, "Deep three-photon imaging of the brain in intact adult zebrafish," *Nat. Methods* **17**(6), 605–608 (2020).
10. M. J. Aragon, A. T. Mok, J. Shea, M. Wang, H. Kim, N. Barkdull, C. Xu, and N. Yapici, "Multiphoton imaging of neural structure and activity in *Drosophila* through the intact cuticle," *eLife* **11**, 1–29 (2022).
11. K. Choe, Y. Hontani, T. Wang, E. Hebert, D. G. Ouzounov, K. Lai, A. Singh, W. Béguelin, A. M. Melnick, and C. Xu, "Intravital three-photon microscopy allows visualization over the entire depth of mouse lymph nodes," *Nat. Immunol.* **23**(2), 330–340 (2022).
12. G. J. Bakker, S. Weischer, J. F. Ortas, J. Heidelin, V. Andresen, M. Beutler, E. Beaurepaire, and P. Friedl, "Intravital deep-tumor single-beam 3-photon, 4-photon, and harmonic microscopy," *eLife* **11**, 1–23 (2022).
13. D. Sinefeld, F. Xia, M. Wang, T. Wang, C. Wu, X. Yang, H. P. Paudel, D. G. Ouzounov, T. G. Bifano, and C. Xu, "Three-Photon Adaptive Optics for Mouse Brain Imaging," *Front. Neurosci.* **16**, 1–10 (2022).

14. H.-H. Lin, X. Tao, J. W. Wang, T. Lam, R. Rodriguez, and J. Kubby, "Transcutaneous imaging with cellular and subcellular resolution," *Biomed. Opt. Express* **8**(3), 1277–1289 (2017).
15. L. Streich, J. C. Boffi, L. Wang, K. Alhalaseh, M. Barbieri, R. Rehm, S. Deivasigamani, C. T. Gross, A. Agarwal, and R. Prevedel, "High-resolution structural and functional deep brain imaging using adaptive optics three-photon microscopy," *Nat. Methods* **18**(10), 1253–1258 (2021).
16. C. Rodríguez, A. Chen, J. A. Rivera, M. A. Mohr, Y. Liang, R. G. Natan, W. Sun, D. E. Milkie, T. G. Bifano, X. Chen, and N. Ji, "An adaptive optics module for deep tissue multiphoton imaging in vivo," *Nat. Methods* **18**(10), 1259–1264 (2021).
17. B. Li, C. Wu, M. Wang, K. Charan, and C. Xu, "An adaptive excitation source for high-speed multiphoton microscopy," *Nat. Methods* **17**(2), 163–166 (2020).
18. T. Wang, C. Wu, D. G. Ouzounov, W. Gu, F. Xia, M. Kim, X. Yang, M. R. Warden, and C. Xu, "Quantitative analysis of 1300-nm three-photon calcium imaging in the mouse brain," *eLife* **9**, 1–22 (2020).
19. A. T. Mok, J. Shea, C. Wu, F. Xia, R. Tatarsky, N. Yapiçi, and C. Xu, "Spatially resolved measurements of ballistic and total transmission in microscale tissue samples from 450 nm to 1624 nm," *Biomed. Opt. Express* **13**(1), 438–451 (2022).
20. B. A. Wilt, J. E. Fitzgerald, and M. J. Schnitzer, "Photon shot noise limits on optical detection of neuronal spikes and estimation of spike timing," *Biophys. J.* **104**(1), 51–62 (2013).
21. A. K. LaViolette and C. Xu, "Shot noise limits on binary detection in multiphoton imaging," *Biomed. Opt. Express* **12**(11), 7033–7048 (2021).
22. C. Xu, W. Zipfel, J. B. Shear, R. M. Williams, and W. W. Webb, "Multiphoton fluorescence excitation: New spectral windows for biological nonlinear microscopy," *Proc. Natl. Acad. Sci. U. S. A.* **93**(20), 10763–10768 (1996).
23. S. Maiti, J. B. Shear, R. M. Williams, W. R. Zipfel, and W. W. Webb, "Measuring serotonin distribution in live cells with three-photon excitation," *Science* **275**(5299), 530–532 (1997).
24. A. P. Davey, E. Bourdin, F. Henari, and W. Blau, "Three photon induced fluorescence from a conjugated organic polymer for infrared frequency upconversion," *Appl. Phys. Lett.* **67**(7), 884–885 (1995).
25. G. S. He, B. A. Reinhardt, J. D. Bhawalkar, and P. N. Prasad, "Three-photon-absorption-induced fluorescence and optical limiting effects in an organic compound," *Opt. Lett.* **20**(14), 1524–1546 (1995).
26. G. Xing, S. Chakraborty, S. W. Ngiam, Y. Chan, and T. C. Sum, "Three-photon absorption in seeded CdSe/CdS nanorod heterostructures," *J. Phys. Chem. C* **115**(36), 17711–17716 (2011).
27. J. D. Bhawalkar, G. S. He, and P. N. Prasad, "Three-photon induced upconverted fluorescence from an organic compound: application to optical power limiting," *Opt. Commun.* **119**(5-6), 587–590 (1995).
28. L.-C. Cheng, N. G. Horton, K. Wang, S.-J. Chen, and C. Xu, "Measurements of multiphoton action cross sections for multiphoton microscopy," *Biomed. Opt. Express* **5**(10), 3427–3433 (2014).
29. Y. Hontani, F. Xia, and C. Xu, "Multicolor three-photon fluorescence imaging with single-wavelength excitation deep in mouse brain," *Sci. Adv.* **7**(12), 1–11 (2021).
30. M. Drobizhev, A. Rebane, Z. Suo, and C. W. Spangler, "One-, two- and three-photon spectroscopy of π -conjugated dendrimers: Cooperative enhancement and coherent domains," *J. Lumin.* **111**(4), 291–305 (2005).
31. X. Deng, Z. Zhuang, H. Liu, P. Qiu, and K. Wang, "Measurement of 3-photon excitation and emission spectra and verification of Kasha's rule for selected fluorescent proteins excited at the 1700-nm window," *Opt. Express* **27**(9), 12723–12731 (2019).
32. H. Liu, X. Deng, S. Tong, C. He, H. Cheng, Z. Zhuang, M. Gan, J. Li, W. Xie, P. Qiu, and K. Wang, "In Vivo Deep-Brain Structural and Hemodynamic Multiphoton Microscopy Enabled by Quantum Dots," *Nano Lett.* **19**(8), 5260–5265 (2019).
33. H. Liu, J. Wang, X. Peng, Z. Zhuang, P. Qiu, and K. Wang, "Ex and in vivo characterization of the wavelength-dependent 3-photon action cross-sections of red fluorescent proteins covering the 1700-nm window," *J. Biophotonics* **11**(7), 1–7 (2018).
34. W. J. Meath and E. A. Power, "On the importance of permanent moments in multiphoton absorption using perturbation theory," *J. Phys. B: At. Mol. Phys.* **17**(5), 763–781 (1984).
35. C. Xu and W. W. Webb, "Multiphoton excitation of molecular fluorophores and nonlinear laser microscopy," in *Topics in Fluorescence Spectroscopy*, J. R. Lakowicz, ed. (Plenum Press, 2002), Vol. 5, pp. 471–540.
36. C. Xu and W. W. Webb, "Measurement of two-photon excitation cross sections of molecular fluorophores with data from 690 to 1050 nm," *J. Opt. Soc. Am. B* **13**(3), 481–491 (1996).
37. J.-C. Diels and W. Rudolph, *Ultrashort Laser Pulse Phenomena*, 2nd ed. (Academic Press, 2006).
38. C. Xu, W. Denk, J. Guild, and W. W. Webb, "Determination of absolute two-photon excitation cross sections by in situ second-order autocorrelation," *Opt. Lett.* **20**(23), 2372–2374 (1995).
39. Semrock, "SearchLight," <https://searchlight.index-hs.com/>.
40. D. J. Segelstein, *The Complex Refractive Index of Water* (University of Missouri-Kansas City, 1981).
41. AG Schott, "Schott optical glass data sheets," https://refractiveindex.info/download/data/2017/schott_2017-01-20.pdf.
42. J. M. Song, T. Inoue, H. Kawazumi, and T. Ogawa, "Determination of two photon absorption cross section of fluorescein using a mode locked titanium sapphire laser," *Anal. Sci.* **15**(6), 601–603 (1999).
43. N. S. Makarov, M. Drobizhev, and A. Rebane, "Two-photon absorption standards in the 550–1600 nm excitation wavelength range," *Opt. Express* **16**(6), 4029 (2008).

44. S. de Reguardati, J. Pahapill, A. Mikhailov, Y. Stepanenko, and A. Rebane, "High-accuracy reference standards for two-photon absorption in the 680-1050 nm wavelength range," *Opt. Express* **24**(8), 9053–9066 (2016).
45. Ohara Corporation, "Ohara Glass Catalog," https://wp.optics.arizona.edu/optomech/wp-content/uploads/sites/53/2016/10/Ohara_Glass_Catalog.pdf.
46. A. K. Rebane and A. Mikhaylov, "Improved reference standards for femtosecond three-photon excitation of fluorescence in the wavelength range 950 - 1750nm," *Proc. SPIE* **1049830**, 10498 (2018).
47. A. Schönle and S. W. Hell, "Heating by absorption in the focus of an objective lens," *Opt. Lett.* **23**(5), 325–327 (1998).
48. A. K. Datta, *Heat and Mass Transfer: A Biological Context*, 2nd ed. (CRC Press, 2017).
49. S. Gigan, O. Katz, and H. B. De Aguiar, *et al.*, "Roadmap on wavefront shaping and deep imaging in complex media," *J. Phys. Photonics* **4**, 1–73 (2022).